TCAD Comprehensive Silicon Strain Model Using Finite Element Quasi-Fermi Discretization

Thomas Weingartner*, Mark E. Law*, Keith Green†, Andrew Thomas*, Henry Johnson*, and Polina Leger*

*The Department of Electrical and Computer Engineering at the University of Florida, Gainesville, USA

† Analog Technology Development, Texas Instruments Dallas, USA

Abstract—In this work we present a finite element quasi-Fermi implementation of a generalized first principles strain model for silicon. Strain effects in silicon are often modeled with separate mobility, bandgap, density of states, piezo-Hall, temperature, and doping models. The current work encompasses these effects by utilizing first principles and the finite element quasi-Fermi method to write a conductivity tensor with the appropriate carrier relationships.

Index Terms—Stress, Silicon, Piezoresistance, Sensors, Strain, Hall, Bipolar Transistors

I. INTRODUCTION

Strain is introduced in many stages of the semiconductor manufacturing process. This can be intentional to improve device performance or unintentional as a result of material property differences on wafer or in package. When a semiconductor product is employed in its application mechanical forces on the silicon chip can be impacted by board soldering or dynamic environmental changes such as temperature and humidity. As a result of these influences strain can undesirably affect the performance of product. Typical strain models consider specific strain configurations and use linear coefficients, such as piezoresistance [1], piezojunction [2], and piezo-Hall [3]. These coefficients then need to be modified for doping and temperature dependence. Other coefficients need to be used for second order effects [4]–[6]. Device simulators implement these linear coefficients with additional bandgap and density of states corrections effects. However, all these effects are derived from first principles theories and these theories can be directly implemented into device simulators. A more advanced model directly implementing the multivalley mobility [7], [8] is present in some device simulators. The model performs similar calculations to those performed in this study but lumps the stress dependence terms into the mobility. This captures temperature and doping dependence but needs additional bandgap and density of states corrections to capture bipolar effects. Its concepts would also have to be extended to include the piezo-Hall effect.

In this study, we implement a first principles silicon strain model in the Florida object-oriented device simulator (FLOODS). The population of carriers is computed in each band and used to compute anisotropic conductivities, which is the key difference between this work and existing multivalley models.

Motivation for development came from the lack of piezo-Hall simulation capabilities in commercial device simulators. Some simulators do not include the effect and other simulators allow the input of the linear piezo-Hall coefficients. An example of piezo-Hall simulation using linear coefficients is seen in the literature [9]. However, implementing the temperature effects of piezo-Hall is non-trivial with the linear coefficient method.

Most Hall devices are electron majority carrier devices, as a result, we will focus on electron transport but some results will pertain to hole calculations. It also would be straight forward to include magneto-resistance and magneto-resistance strain effects within this simulation framework.

For ease of implementation finite element quasi-Fermi (FEQF) discretization was used over the more traditional finite volume Scharfetter-Gummel (FVSG) discretization. However, it is likely that the presented model could be implemented with FVSG discretization or a FVSG-like element. The FEQF system of equations is shown in Eqns. (1), (2), (3), (4). Poisson's equation is shown in Eqn. (1). Ψ is the electrostatic potential, q is the fundamental electric charge, p is the hole concentration, n is the electron concentration, N_D^+ is the donor concentration, N_A^- is the acceptor concentration.

$$\nabla \cdot (\epsilon \nabla \Psi) = -q(p - n + N_D^+ - N_A^-) \quad (1)$$

The electron and hole concentrations are seen in Eqn. (2). Where J is the current density and U is a recombination term.

$$\begin{aligned} \frac{\partial n}{\partial t} &= \frac{1}{q}\nabla \cdot \mathbf{J_n} - U_n \\ \frac{\partial p}{\partial t} &= -\frac{1}{q}\nabla \cdot \mathbf{J_p} - U_p \end{aligned} \quad (2)$$

Current is defined in Eqn. (3). Mobility is represented by μ and quasi-Fermi level is represented by Φ.

$$\begin{aligned} \mathbf{J_n} &= -q\mu_n n\nabla\Phi_n \\ \mathbf{J_p} &= -q\mu_p p\nabla\Phi_p \end{aligned} \quad (3)$$

Electron and hole carrier relationships are in Eqn. (4). We use Fermi-Dirac ($F_{1/2}$) statistics defined at the conduction band edge (E_c) and the valance band edge (E_v). The carrier concentration at the conduction and the valance band edge are defined as N_c and N_v respectively. Temperature (T) and Boltzmann's constant (k) are also present.

$$n = N_c F_{1/2}\left(\frac{E_c - \Phi_n}{kT}\right)$$
$$p = N_v F_{1/2}\left(\frac{\Phi_p - E_v}{kT}\right) \tag{4}$$

The continuous current definition provided by FEQF discretization [10], seen in Eqn. (5), allows for a simple tensor definition of conductivity, where the normal terms describe anisotropic electrostatic transport and shear terms describe the Lorentz force.

$$\mathbf{J_n} = -\begin{bmatrix} \sigma_{xx} & \sigma_{xy} & \sigma_{xz} \\ \sigma_{yx} & \sigma_{yy} & \sigma_{yz} \\ \sigma_{zx} & \sigma_{zy} & \sigma_{zz} \end{bmatrix} \nabla\Phi_n \tag{5}$$

Note that the tensor conductivity in Eqn. (5) is equivalent to the isotropic mobility Eqn. (2) when no magnetic field is present and the diagonal terms are equivalent. This relationship is illustrated in Eqn. (6).

$$\mathbf{J_n} = -\begin{bmatrix} \sigma & 0 & 0 \\ 0 & \sigma & 0 \\ 0 & 0 & \sigma \end{bmatrix} \nabla\Phi_n = -q\mu_n n\nabla\Phi_n \tag{6}$$

Silicon and germanium electron bandstructure and behavior under the influence of strain is well established and has been known since the 1950s [11]–[15]. Silicon has 6 degenerate ellipsoidal shaped valleys near the X-symmetry point. In the $\langle 100 \rangle$ conduction of current, two valleys are considered longitudinal and four are considered transverse. Fig. 1 shows a sketch of the silicon electron Fermi surfaces. The curvature of the valleys is indicative of the effective mass, thus transverse valleys have mobilities about five times larger than longitudinal mobilities. This means the transverse mobilities are about two times larger than the perpendicular mobilities. These factors cause current conduction to be dominated by the four transverse valleys. It should be noted that illustrated in Fig. 1, current induced by the Lorentz force is dominated by the two valleys parallel to the magnetic field since these two valleys have mobilities transverse to the electrostatic and induced current.

II. Methods

Silicon electron transport behavior due to strain (ϵ) can be comprehensively handled with deformation potential theory [11] and accounting for the splitting of transverse mobilities [14]. The deformation potential coefficients, Ξ_u and Ξ_d, calculate the change in band edge energy ΔE in the three principle directions due to strain, seen in Eqn. (7). It should be noted that Ξ_d plays a larger role in bipolar devices where the magnitude of the bandgap change is important. These principle directions are the directions of the six ellipsoids, $\gamma = \{\langle 100 \rangle, \langle 010 \rangle, \langle 001 \rangle\}$. Crystal directions are also shortened with 1 as $\langle 100 \rangle$, 2 as $\langle 010 \rangle$, 3 as $\langle 001 \rangle$.
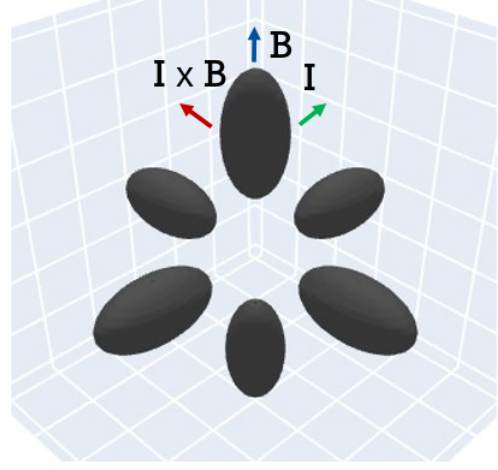
Fig. 1. 3D Fermi surface sketch of the six electron valleys in silicon. Each ellipsoid is aligned along $\langle 100 \rangle$, $\langle 010 \rangle$, $\langle 001 \rangle$, $\langle \bar{1}00 \rangle$, $\langle 0\bar{1}0 \rangle$, $\langle 00\bar{1} \rangle$. We consider ellipsoids along the same axis to be degenerate yielding three ellipsoids for carrier concentration calculations. An example of the Lorentz force in the dominate ellipsoid is shown.

$$\begin{bmatrix} \Delta E_1 \\ \Delta E_2 \\ \Delta E_3 \end{bmatrix} = \begin{bmatrix} \Xi_u + \Xi_d & \Xi_d & \Xi_d \\ \Xi_d & \Xi_u + \Xi_d & \Xi_d \\ \Xi_d & \Xi_d & \Xi_u + \Xi_d \end{bmatrix} \begin{bmatrix} \epsilon_{11} \\ \epsilon_{22} \\ \epsilon_{33} \end{bmatrix} \tag{7}$$

This change in energy redistributes the population of electrons between the six ellipsoidal electron conduction bands. Eqn. (8) gives carrier relationships using Fermi statistics to calculate the carrier concentrations in the 3 principle directions, n_γ.

$$n_\gamma = N_c * F_{1/2}((E_c - F_n - \Delta E_\gamma)/V_t) \tag{8}$$

Each of the three non-degenerate ellipsoids contributes to the conduction of electrons with a different effective mass depending on if the current is parallel (m_l^*) or transverse (m_t^*) to the major axis of the ellipsoid. These longitudinal and transverse effective masses are used to calculate the respective longitudinal (μ_l) and transverse (μ_t) mobilities. When strain redistributes the electrons between conduction bands, the conductivity is changed from the reweighting of the different mobilities, seen in Eqn. (9). The nature of the reweighting gives three different uniaxial conductivities (σ_{11}, σ_{22}, σ_{33}).

$$\begin{bmatrix} \sigma_{11} \\ \sigma_{22} \\ \sigma_{33} \end{bmatrix} = \begin{bmatrix} \mu_l & \mu_t & \mu_t \\ \mu_t & \mu_l & \mu_t \\ \mu_t & \mu_t & \mu_l \end{bmatrix} \begin{bmatrix} n_1 \\ n_2 \\ n_3 \end{bmatrix} \tag{9}$$

The relaxation time ($\langle \tau \rangle$) in each ellipsoid changes with the bend edge shift [3], [16], [17]. Though the effective masses (m^*) are constant for electrons under uniaxial strain, the

mobility is modified through this relaxation time shift in Eqn. (10).

$$\mu_\gamma = \frac{q\langle\tau\rangle_\gamma}{m^*} \quad (10)$$

The change in relaxation time can be approximated as a linear shift with energy related through a proportionality constant $f = 10eV^{-1}$ [3].

$$\frac{\Delta\langle\tau\rangle_\gamma}{\langle\tau\rangle_0} = \frac{2}{3}f\Delta E_\gamma \quad (11)$$

Shear strain induces a splitting in the transverse mobilities in ellipsoids whose major axis is perpendicular to the shear plane. An example of this would be $m_{t_3} = 1\pm\alpha_0\epsilon_{12}$, where $\alpha = 86.8$ [14]. This is an important correction when considering crystal orientation other than the principle axes of $\langle100\rangle\langle001\rangle$.

Choice of deformation potential constants is difficult as there exists many measured values in the literature [11], [18]–[20], as well as many others not cited. Table I gives the choice of constants used for the piezo-Hall and piezojunction results. There seems to be broad agreement on the effective mass values. However in Kanda's work [20], the deformation potential parameters $\Xi_u = 8.5$ and $\Xi_d = -5.2$ are used. These are substantially different and give different results for the piezo-Hall effect. This is why in replicating Kanda's temperature dependences we use his deformation potential parameters and all other results we use the values given in Table I.

TABLE I
CONSTANTS

Const	Value	Reference
Ξ_u	10.5	[19]
Ξ_d	1.1	[19]
m_l^*/m^*	0.9161	[14]
m_t^*/m^*	0.1905	[14]

When magnetic field is introduced, terms that appear as shear conductivities (σ_{23}, σ_{13}, σ_{12}) account for the Lorentz force. This force is both perpendicular to electrostatic current flow and the magnetic field (**B**), where B_1, B_2, B_3 are the components of the magnetic field along the crystal axes. Thus the behavior of the current induced by the Lorentz force is controlled by both the mobility in the electrostatic current direction as well as the induced direction. A similar relationship to the electrostatic conductivities is written in Eqn. (12). Here the off diagonals correspond to ellipsoids parallel to electrostatic current flow and perpendicular to induced current flow or vice versa. However, conduction is dominated by the diagonal terms where both the electrostatic and induced currents are perpendicular to the ellipsoid ($\mu_t^2 \gg \mu_t * \mu_l$).

$$\begin{bmatrix} \sigma_{23} \\ \sigma_{13} \\ \sigma_{12} \end{bmatrix} = \begin{bmatrix} \mu_t^2 B_1 & \mu_l\mu_t B_1 & \mu_l\mu_t B_1 \\ \mu_l\mu_t B_2 & \mu_t^2 B_2 & \mu_l\mu_t B_2 \\ \mu_l\mu_t B_3 & \mu_l\mu_t B_3 & \mu_t^2 B_3 \end{bmatrix} \begin{bmatrix} n_1 \\ n_2 \\ n_3 \end{bmatrix} \quad (12)$$

Using the Lorentz force and the right hand rule the conductivities are skew symmetric. Using this property we can formulate the conductivity tensor seen in Eqn. (13).

$$\sigma_{ij} = \begin{bmatrix} \sigma_{11} & \sigma_{12} & -\sigma_{13} \\ -\sigma_{12} & \sigma_{22} & \sigma_{23} \\ \sigma_{13} & -\sigma_{23} & \sigma_{33} \end{bmatrix} \quad (13)$$

The conductivity tensor allows us to easily write our FEQF transport in Eqn. (14). This conductivity tensor when coupled with Poisson's equation accounts for mobility, density of states, and bandgap changes.

$$-\nabla \cdot (\sigma_{ij}\nabla F_n) = \frac{\partial n}{\partial t} \quad (14)$$

Until now we have assumed that the simulation axes (x, y, z) have lined up with the axes of the crystal ($\langle100\rangle, \langle010\rangle, \langle001\rangle$). To simulate different crystal orientations the conductivity and deformation potentials tensors must be rotated.

The same general ideas behind this model can be extended to hole simulation. However, hole simulation is more complex than electron simulation because the effective masses change for both light and heavy holes. As of the writing of this paper only certain crystal orientations have been implemented. Bandgap and density of states changes have been extracted from the LK Hamiltonian [21]. Mobilities for specific crystal orientations have been taken from [22]. Hole relaxation time effects have not been considered. Using these parameters a similar conductivity tensor can be written to describe hole behavior.

III. RESULTS

Validation of this model can be done by comparing results against simulations done with the piezoresistance, piezo-Hall, and piezojunction effects. An example of the linear piezoresistance (π) relationship between resistivity (ρ) and stress (s) is shown in Eqn. (15).

$$\begin{bmatrix} \frac{\Delta\rho_{11}}{\rho} \\ \frac{\Delta\rho_{22}}{\rho} \\ \frac{\Delta\rho_{33}}{\rho} \end{bmatrix} = \begin{bmatrix} \pi_l & \pi_t & \pi_t \\ \pi_t & \pi_l & \pi_t \\ \pi_t & \pi_t & \pi_l \end{bmatrix} \begin{bmatrix} s_{11} \\ s_{22} \\ s_{33} \end{bmatrix} \quad (15)$$

Both the piezoresistance model and this work modify the conductivity. The piezoresistance model simply modifies the value of the conductivity in a certain direction. While this work modifies the carrier relationships and mobilities to yield an effective conductivity change.

Piezoresistance and piezo-Hall factors are extracted to show the inclusion of temperature and doping effects. These factors multiply either of these linear coefficients to give the doping and temperature dependence. The goal is to show temperature and doping effects are included inherently without the need to modify any equations.

A. Piezoresistance

Extracted piezoresistance coefficients at 50 MPa along with values from Kanda's paper are seen in Table II. Discrepancies between Kanda's values and this work are attributable to the inclusion of second order effects [4], [6], [20] and the choice of deformation potential constants.

TABLE II
PIEZORESISTANCE COEFFICIENTS (% / 100 MPA)

| | π_l | | π_t | |
Crystal Orientation	Kanda	This Work	Kanda	This Work
$\langle 100 \rangle (001)$	-10.2	-9.0	5.3	5.4
$\langle 110 \rangle (001)$	-3.1	-2.3	-1.8	-1.4

Fig. 2 compares FLOOXS simulated normalized π_{11} coefficient temperature and doping dependence to the same "Piezoresistance factor" derived by Kanda [1].
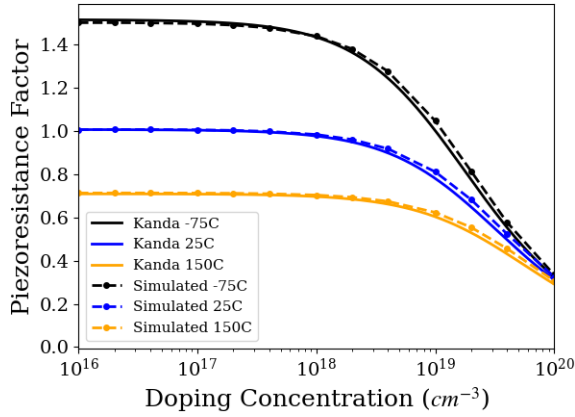
Fig. 2. Comparison of Kanda piezoresistance temperature dependence calculation and FLOODS simulation piezoresistance extraction. A 1um x 1um grid with $1 \times 10^{16} cm^{-3}$ uniform doping was used for the calculation.

B. Piezo-Hall

Fig. 3 shows the temperature and dopant concentration dependences of the piezo-Hall factor. Some numerical noise is evident at high temperatures and high doping. The inset of Fig. 3 gives the normalized temperature dependence of the piezo-Hall effect for a simple square n-type sensor. This is a new result as no computed temperature dependence of the piezo-Hall effect is seen in the literature.

C. Piezojunction

Fig 4. gives the nonlinear response of a bipolar transistor's collector current broken up into the mobility and n_i components. The ability of the model to calculate mobility changes has been extensively discussed. This result is included to show the model completely captures the bandgap narrowing and density of states changes through its formulation. The n_i term contains the nonlinear response of the bandgap and density of states changes. The bandgap and density of states changes are
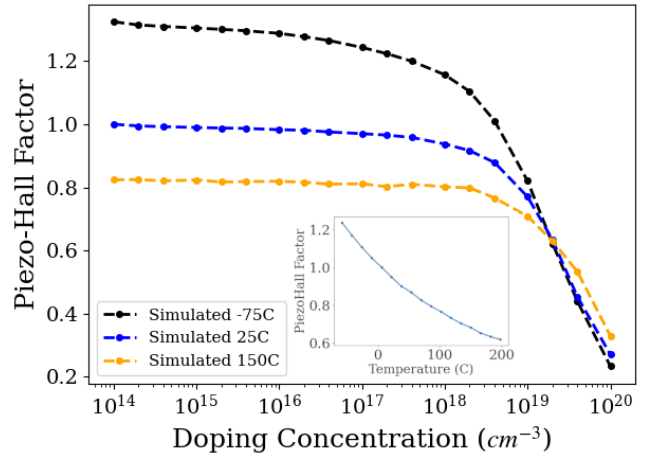
Fig. 3. FLOODS simulation piezo-Hall extraction with doping concentration and temperature. Inset shows temperature dependence at low doping values.

nonlinear with similar trends in both tensile and compressive stress but different magnitudes. This is evident in the parabolic nature of the n_i curve.
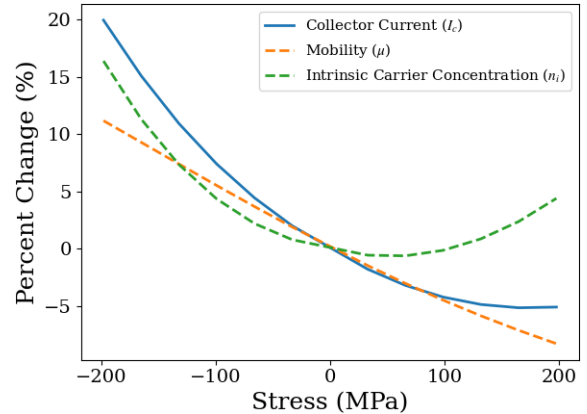
Fig. 4. Bipolar transistor collector current vs stress. The constituent components of the collector current change are shown as the extracted mobility change (μ) and intrinsic carrier concentration change (n_i)

IV. CONCLUSIONS

We have implemented a new TCAD comprehensive strain model in FLOODS capable of simulating strain effects in unipolar, bipolar, and Hall devices. This model produces results consistent with existing models and for the first time has been able to investigate temperature dependence of the piezo-Hall effect on a 3D structure. By implementing first principles bandstructure information within the device simulator we are able to account for temperature and doping dependence without needing additional corrections.

Aravind Appaswamy at TI for discussions on bipolar devices and Scott Thompson at the University of Florida for general discussions on strain effects.

REFERENCES

[1] Y. Kanda, "A graphical representation of the piezoresistance coefficients in silicon," vol. 29, no. 1, pp. 64–70.

[2] J. Creemer, F. Fruett, G. Meijer, and P. French, "The piezojunction effect in silicon sensors and circuits and its relation to piezoresistance," vol. 1, no. 2, p. 98.

[3] B. Hälg, "Piezo-hall coefficients of n-type silicon," vol. 64, no. 1, pp. 276–282.

[4] K. Matsuda, K. Suzuki, K. Yamamura, and Y. Kanda, "Nonlinear piezoresistance effects in silicon," vol. 73, no. 4, pp. 1838–1847.

[5] K. Matsuda, Y. Kanda, K. Yamamura, and K. Suzuki, "Second-order piezoresistance coefficients of p-type silicon," vol. 29, pp. L1941–L1942.

[6] K. Matsuda, Y. Kanda, and K. Suzuki, "Second-order piezoresistance coefficients of n-type silicon," vol. 28, pp. L1676–L1677.

[7] S. Dhar, H. Kosina, G. Karlowatz, S. E. Ungersboeck, T. Grasser, and S. Selberherr, "High-field electron mobility model for strained-silicon devices," vol. 53, no. 12, pp. 3054–3062.

[8] E. Ungersboeck, S. Dhar, G. Karlowatz, H. Kosina, and S. Selberherr, "Physical modeling of electron mobility enhancement for arbitrarily strained silicon," vol. 6, no. 1, pp. 55–58.

[9] T. Kaufmann, D. Kopp, M. Kunzelmann, P. Ruther, and O. Paul, "Piezo-hall effect in CMOS-based vertical hall devices," in *2011 IEEE SENSORS Proceedings*, pp. 440–443, IEEE.

[10] D. J. Cummings, M. E. Law, S. Cea, and T. Linton, "Comparison of discretization methods for device simulation," in *2009 International Conference on Simulation of Semiconductor Processes and Devices*, pp. 1–4, IEEE.

[11] C. Herring and E. Vogt, "Transport and deformation-potential theory for many-valley semiconductors with anisotropic scattering," vol. 101, no. 3, pp. 944–961.

[12] L. Kleinman, "Deformation potentials in silicon. II. hydrostatic strain and the electron-phonon interaction," vol. 130, no. 6, pp. 2283–2289.

[13] I. Goroff and L. Kleinman, "Deformation potentials in silicon. III. effects of a general strain on conduction and valence levels," vol. 132, no. 3, pp. 1080–1084.

[14] J. C. Hensel, H. Hasegawa, and M. Nakayama, "Cyclotron resonance in uniaxially stressed silicon. II. nature of the covalent bond," vol. 138, no. 1, pp. A225–A238.

[15] I. Balslev, "Influence of uniaxial stress on the indirect absorption edge in silicon and germanium," vol. 143, no. 2, pp. 636–647.

[16] F. J. Morin, T. H. Geballe, and C. Herring, "Temperature dependence of the piezoresistance of high-purity silicon and germanium," vol. 105, no. 2, pp. 525–539.

[17] O. N. Tufte and E. L. Stelzer, "Piezoresistive properties of heavily doped n-type silicon," vol. 133, no. 6, pp. A1705–A1716.

[18] R. N. Dexter, H. J. Zeiger, and B. Lax, "Cyclotron resonance experiments in silicon and germanium," vol. 104, no. 3, pp. 637–644.

[19] M. V. Fischetti and S. E. Laux, "Band structure, deformation potentials, and carrier mobility in strained si, ge, and SiGe alloys," vol. 80, no. 4, pp. 2234–2252.

[20] Y. Kanda, "Piezoresistance effect of silicon," vol. 28, no. 2, pp. 83–91.

[21] A. Dargys, "Luttinger-kohn hamiltonian and coherent excitation of the valence-band holes," vol. 66, no. 16, p. 165216.

[22] K. Matsuda, "Strain-dependent hole masses and piezoresistive properties of silicon," p. 4.